Multiple scattering identification in spaceborne W-band radar measurements of deep convective cores

Multiple scattering identification in spaceborne W-band radar measurements of deep convective cores

A. Battaglia,[1] T. Augustynek,[1] S. Tanelli,[2] and P. Kollias[3]

Received 21 April 2011; revised 5 July 2011; accepted 12 July 2011; published 4 October 2011.

[1] CloudSat observations have indicated that multiple scattering affects 94 GHz spaceborne radar observations. The ESA EarthCARE explorer mission scheduled to launch in 2015 features also a spaceborne 94-GHz radar with Doppler capability for providing a global data set of convective motions and particle sedimentation rates. Vertical velocity measurements will be collected in all cloud conditions, including deep convection where multiple-scattering is expected to contaminate the signal. Thus, before the spaceborne Doppler radars are used for science application, it is imperative to develop a method to identify radar range gates contaminated by multiple scattering contributions. Based on simulations, a criterion to identify the onset of multiple scattering is presented in this paper; the cumulative integrated reflectivity from the top of the atmosphere is a proxy of the multiple scattering enhancement and can be confidently used to detect the onset of multiple scattering. Analysis of a limited (two months) CloudSat data set reveals that, for deep tropical convective cores, the onset of significant multiple scattering typically occurs in the region between 9–10 km and more than 35% of the range bins above the freezing level height and with reflectivity above −20 dBZ are not affected by multiple scattering. This assessment offers a conservative upper limit for EarthCARE 94-GHz radar multiple scattering effects due to the narrower field of view of the Doppler radar compared to CloudSat's radar. Identification of multiple scattering contamination in the CloudSat and EarthCARE radar observations facilitates the following objectives: (1) to constrain the region of validity of currently developed CloudSat products based on single scattering theory (e.g. 2B-CWC-RO, 2B-CWC-RVOD) and (2) to filter out multiple scattering affected range bins in any analysis aimed at the assessment of the feasibility and of the accuracy of the EarthCARE Doppler estimates within deep convective cores.

Citation: Battaglia, A., T. Augustynek, S. Tanelli, and P. Kollias (2011), Multiple scattering identification in spaceborne W-band radar measurements of deep convective cores, *J. Geophys. Res.*, *116*, D19201, doi:10.1029/2011JD016142.

1. Introduction

[2] Deep convection plays a key role in the exchange between the upper troposphere and the lower stratosphere with important consequences for the energy and heat budget [*Tian and Ramanathan*, 2002; *Kuang and Bretherton*, 2004] and moisture distribution [e.g., *Sohn and Schmetz*, 2004]. However, the role played by deep cloud intrusions through the tropopause remains controversial: convective overshooting clouds can cause both hydration [*Corti et al.*, 2008; *Jensen et al.*, 2007] and dehydration [*Sherwood and Dessler*, 2001] of the stratosphere, depending on the characteristic size of the ice particles, which determines sedimentation rates. Moreover, the more intense the convection the larger the potential for mass exchange in the tropical tropopause layer [*Liu and Zipser*, 2005]. This requires to quantify how intense deep convection is, viz how strong updraft velocities are and at which altitudes they appear. "Deep" convection may be generated in different environments and may therefore occur with different convective intensities. Figure 12 of *Liu et al.* [2008] demonstrates substantial differences between the updraft strength of Central Africa and the northwestern tropical Pacific convective systems. *Liu et al.* [2008] conclude that the strong and/or long lasting convective system updrafts, observed frequently over land, are more likely to reach criteria for the mesoscale convective complex size, duration, and shape by spreading sufficient condensate into anvils.

[3] The challenges and limitations associated with high-altitude aircraft overflights or penetrations in convective cloud tops along with the need for global data sets suggests that space-borne based vertical velocity measurements are needed. Thermal infrared window channel measurements are widely used to investigate the distribution and intensity

[1]Department of Physics and Astronomy, University of Leicester, Leicester, UK.
[2]Jet Propulsion Laboratory, California Institute of Technology, Pasadena, California, USA.
[3]Department of Atmospheric and Oceanic Sciences, McGill University, Montreal, Quebec, Canada.

0148-0227/11/2011JD016142

of tropical deep convection but they are inherently affected by misclassification problems, especially related to the presence of cold and/or thick cirrus anvils [*Liu et al.*, 2007] and to optically thin upper layers [*Sherwood et al.*, 2004]. Observations with the TRMM precipitation radar (PR) operating at 13.8 GHz represent a significant leap forward in the understanding of deep convection; by combining vertical radar profiles with IR cloud top temperatures *Liu and Zipser* [2005] show that overshooting convection is more frequent over land than over water with hot spots over central Africa, Indonesia, and South America. Convection over central Africa provides by far the largest contribution of overshooting area, volume and precipitating ice mass. 1.3% of tropical convection systems have reflectivities larger than 20 dBZ at altitudes higher than 14 km and 0.1% of all systems may even penetrate the 380 K potential temperature level, identified as the climatological tropopause.

[4] Unfortunately when studying the vertical structure of cloud systems with the TRMM radar a significant vertical portion of the upper part of convective cloud tops is undetected by the PR. For instance only 1% of the cloud area having 11 μm brightness temperature colder than 210 K coincides with TRMM-PR profiles with the 20-dBZ-level reaching 14 km. This implies that the distance between cloud top and maximum 20-dBZ height is often 6 km or even greater [*Liu et al.*, 2007]. The CloudSat mission [*Stephens et al.*, 2008] with its 94 GHz nadir pointing Cloud Profiling Radar (CPR) provides a new observational paradigm for convection studies. Due to its high sensitivity (down to −30 dBZ as shown by *Tanelli et al.* [2008]), the CPR provides a much more detailed vertical structure of cloud tops and water contents than the TRMM PR, but is affected by the obviously larger attenuation and multiple scattering (MS hereafter) which limit its usefulness to the upper portion of deep convection. The collocated observations of the CPR with other instruments of NASA's A-Train satellite constellation foster numerous convective cloud studies. *Chung et al.* [2008] demonstrate that warmer water vapor pixels are associated with convective clouds whose tops are located above 14 km. By combining CloudSat, MODIS and ECMWF data *Luo et al.* [2008] demonstrate the possibility of studying the life of an overshoot and of subdividing it into growing, mature and dissipating stages. Overshooting convection is not a rare phenomenon but represents about 2% of the pixels identified as deep convection by the 2B-CLDCLASS in the ‐20° to 20° latitude belt. With the suite of the A-Train instruments *Iwasaki et al.* [2010] performed a case study of an overshooting cloud and demonstrated its potential to hydrate the stratosphere. Despite all these improvements, the direct measure of convective intensity on a global scale still eludes the community because none of the aforementioned instruments can measure vertical velocity.

[5] The Earth Clouds, Aerosols and Radiation Explorer (EarthCARE, hereafter EC) mission with a spaceborne 94 GHz cloud profiling radar (EC-CPR) on-board is intended for launch in 2016. The EC-CPR is expected to provide the atmospheric sciences community with radar reflectivity measurements at the same frequency, and improved resolution and sensitivity, as the 94 GHz CloudSat's CPR. EC-CPR will also be the first spaceborne cloud radar with Doppler capability: mean Doppler velocity measurements can enable algorithms for a more accurate characterization of clouds and precipitation (classification, retrieval accuracy, monitoring of dynamics, etc.). In deep convection EC-CPR is expected to provide independent estimates of the cloud top height and convective intensity using the Doppler measurements, an unprecedented measurement for this kind of system.

[6] Achieving useful Doppler accuracy (e.g. of the order of 1 m/s at 1 km along-track integration for convection) with EC's 2.5 m antenna and standard processing algorithms, especially in the case of convection, will be challenging. The five primary factors that control the performance of EC-CPR Doppler measurements in deep convective clouds are outlined below:

[7] 1. High specific attenuation at 94 GHz limits the top-down penetration of the radar signal only to the upper portion of convective cores. For instance, based on collocated CloudSat and RASTA 94 GHz airborne radar measurements, *Protat et al.* [2009] conclude that their CloudSat convective ice profiles can be used down to approximately 9 km height (or 4 km above the melting layer) without attenuation correction but below such level they need to be corrected for attenuation by supercooled liquid water and ice aggregates/graupel particles and MS prior to their quantitative use.

[8] 2. Higher-order scattering contributions can overwhelm the single scattering (SS hereafter) signal with subsequent detrimental effects for the retrieval [*Battaglia et al.*, 2010; *Haynes et al.*, 2009, and references therein].

[9] 3. The low Nyquist velocity (related to pulse repetition frequency, for EC-CPR in the range 4.8–6 m/s) in conjunction with the spectra broadening term introduced by the satellite motion (equal to 3.2 m/s for the EC-CPR antenna in uniform beam filling conditions) introduces large uncertainties in the Doppler velocity estimates from space [*Tanelli et al.*, 2002a].

[10] 4. Due to the strong horizontal non-uniformity present in convective cores nonuniform beam filling introduces mean Doppler velocity biases [*Tanelli et al.*, 2002a, 2004; *Schutgens*, 2008a, 2008b].

[11] 5. Several factors like attitude determination errors, thermal distortions of the antenna support, vibrations due to moving parts, slew, thermal flutter or thermal snaps introduce an antenna pointing error. For nadir-pointing systems such errors are negligible only if the antenna is in the cross-track plane, i.e. when the antenna pointing and the spacecraft directions are orthogonal. The pointing uncertainty can be estimated by measuring the apparent velocity of the surface. While the corrections are quite straightforward over sea surfaces (with homogeneous normalized surface radar cross section) and when the radar is observing a homogeneous field, things become very complicated in presence of nonuniform beam filling (NUBF) and sophisticated techniques are needed [e.g., *Tanelli et al.*, 2005].

[12] If standard processing algorithms (pulse pair or discrete Fourier Transform [*Tanelli et al.*, 2002b]) are used, gaps in velocity information are expected, especially in regions of strong convection, hurricanes and regions of high horizontal variability of the cloud and precipitation fields. The goal of this paper is to discuss in detail the first two issues and to identify methods suitable for future algorithms, whereas the last three issues will be topic of a follow up study.

Table 1. Configuration for CloudSat and EarthCARE Spaceborne Radars

Configuration	Frequency	Altitude	Beam Width	Vertical Resolution	PRF Range
EarthCARE	94.0 GHz	395 km	0.08°	500 m	6000 ÷ 7500 Hz
CloudSat *W*	94.0 GHz	705 km	0.1°	500 m	3700 ÷ 4300 Hz

[13] For spaceborne millimeter wavelength radars MS and attenuation are two different manifestations of the same underlying phenomenon, i.e. the multiple interaction of the emitted radiation within the radar field of view [*Battaglia et al.*, 2010]. In the CloudSat CPR observations MS is ubiquitous particularly in presence of deep convection because then larger ice contents and ice particles are more likely to occur. In fact, looking at the geographical distribution for the CloudSat data set, the patterns of MS contaminated regions mirror those of convective areas [*Battaglia et al.*, 2008a, Figures 9–11]. *Battaglia et al.* [2008a] propose a flagging criterion for MS-contaminated profiles that relies on the path integrated attenuation estimated via the surface reference technique, a product available in the 2B-GEOPROF (details at www.cloudsat.cira.colostate.edu/dataSpecs.php). This approach has two weaknesses: first, it does flag the entire radar profile (and not only the ranges that are MS contaminated); second, the approach depends on path integrated attenuation estimates, that are available only over sea (where it has a typical 2 dB error) and can be very misleading in regions of strong nonuniform beam filling (likely to happen in convection).

[14] The goal of this study is to narrow down to what altitude the SS approximation remains valid, i.e. to identify criteria based on the reflectivity profile alone for flagging MS-contaminated radar-ranges. This is a timely effort both for the evaluation and further development of CloudSat products (e.g. estimates of ice water content in mesoscale convective systems) and in preparation of the EarthCARE mission (e.g. characterization of the accuracy in mean Doppler velocities). A comparison of the CloudSat and EarthCARE CPR technical specifications can be found in Table 1.

[15] Section 2 describes the end-to-end simulator with focus on its forward component and a convective scenario is used to illustrate the forward model outputs in Section 3. An objective methodology for the identification of MS-contaminated range-bins purely based on reflectivity profile-derived variables is proposed in Section 4 for the CloudSat and EarthCARE configuration. The operational thresholds are then applied in a case study to CloudSat observations and global statistics of the occurrence of MS are reported in Section 5. Discussions and conclusions are then drawn in Section 6.

2. Description of Forward Modeling

[16] An end-to-end simulator for spaceborne Doppler radars has been developed within the framework of collaborative projects (the ESA funded DAME "Doppler Air Motion Estimate" and the NASA funded DOVE "Doppler Velocity products for the EarthCARE mission"). The simulator capitalizes on the existing EarthCARE simulator [*Voors et al.*, 2007] developed for the EarthCARE mission but significantly improves its radar forward and instrument model. The forward model includes a Monte Carlo module (the Doppler Multiple Scattering simulator) which accounts for MS, polarization of the radar emitted and received radiation and interaction with a Kirchoff-type surface [*Battaglia and Tanelli*, 2011]. Hydrometeors (cloud ice, cloud water, rain, graupel and snow) are modeled as spheres with exponential size distributions. Graupel and snow densities are assumed to be 0.4 and 0.1 g/cm^3. The model has been developed on previous simulators capable of accounting for MS [*Battaglia et al.*, 2007; *Battaglia and Simmer*, 2008; *Battaglia et al.*, 2008b]. The forward unit computes the cross and co-polar reflectivities including all scattering order contributions and the ideal radar Doppler spectra (sampled at very high PRF, a multiple of the real PRF) as measured by a spaceborne radar flying over 3D highly resolved scenes produced via Weather Research and Forecasting Model (WRF) simulations [*Skamarock et al.*, 2005]. In this context, "ideal" means that no Doppler aliasing or second trip echoes affect the signal. The output Doppler spectra result from the combined effect of the satellite velocity and the hydrometeor/wind speeds in the volume under observation accounting for the viewing geometry and the antenna pattern [*Tanelli et al.*, 2002a]. From the idealized forward model output the instrument model derives the signal fluctuations measured at the radar antenna port (i.e., the in-phase and quadrature sample time series) as shown by *Tanelli et al.* [2002b], including signal fluctuation and thermal noise [*Zrnić* 1975] and from these, the estimates of the Doppler moments via the pulse pair technique [*Sirmans and Bumgarner*, 1975]. A schematic for the overall procedure is depicted in Figure 1. The signal processing component is better described in a future paper.

3. Forward Model Results for Simulated Convective Scenarios: Relevance of MS

[17] The end-to-end simulator is applied to a convective scenario produced by a 0.33-km horizontal resolution WRF simulation for the EC-CPR configuration of Table 1 [*Parodi and Tanelli*, 2010]. The vertical cross section of the precipitating scene is shown in Figure 2. The top left panel shows the precipitating hydrometeor content taken from the WRF model while on the right panel the mean Doppler velocity (resulting from the hydrometeor fall speed and the air vertical motion, no radar geometry or satellite motion is introduced) is plotted. There is a considerable updraft (up to 10 m s^{-1}) in the region between 6 and 12 km in the mid-high troposphere, which clearly highlights the presence of a convective core. MS reflectivities and MS Doppler velocities are shown in the middle panels of Figure 2. White pixels correspond to signal smaller than −40 dBZ, which is treated as noise level for all configurations. Considerable attenuation is produced in correspondence to the convective core. As expected, at 94 GHz the attenuation is quite pronounced and reflectivities never exceed 20 dBZ due to non-Rayleigh effects [*Kollias et al.*, 2007]. Strong signal attenuation leads to complete disappearance of the surface echo in large portion of the simulation. MS enhancement is clearly present (bottom left panel) and generally extends the regions where the signal stays above the noise level. Close to the

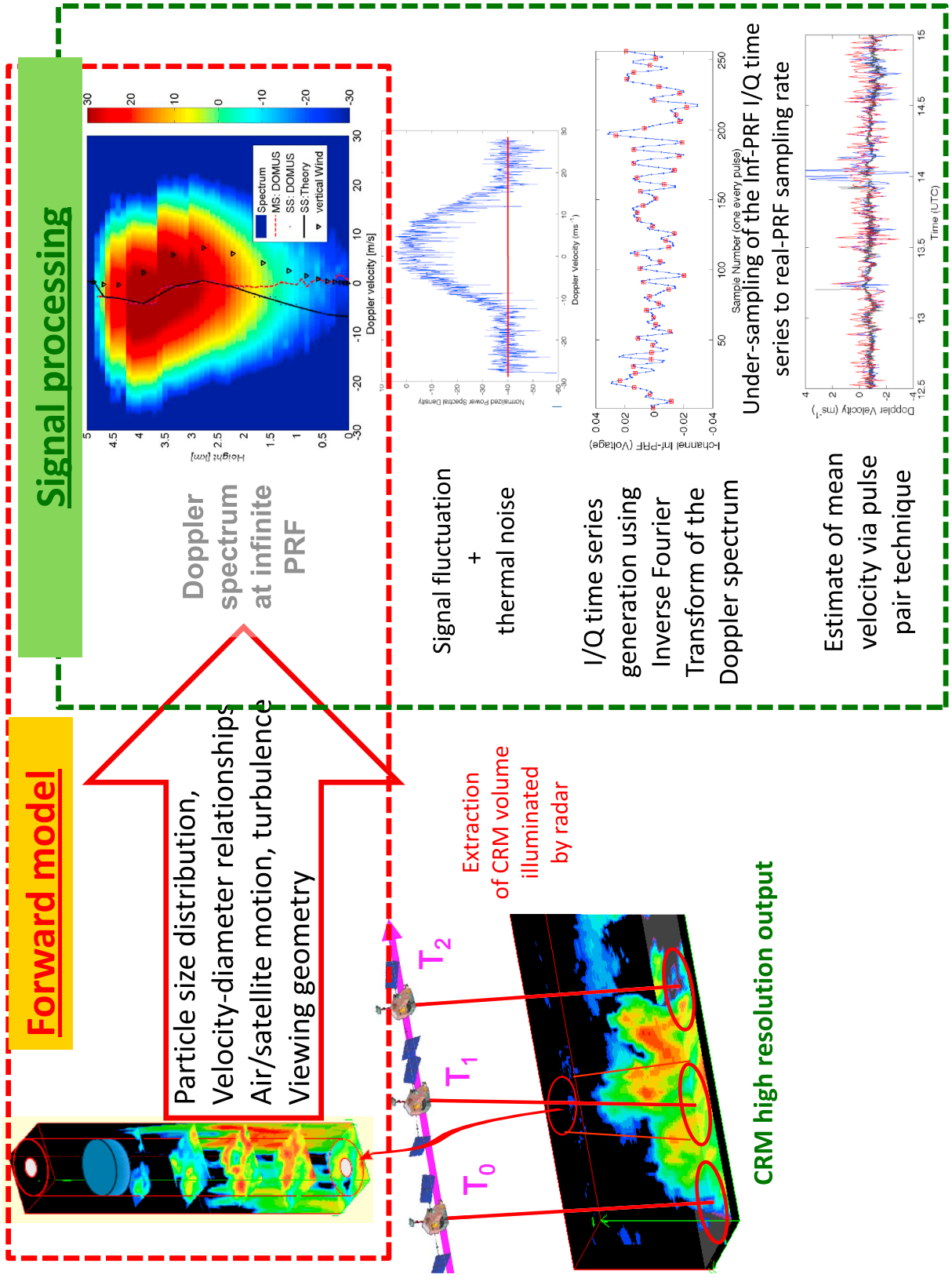

Figure 1. Schematic of the end-to-end DAME simulator.

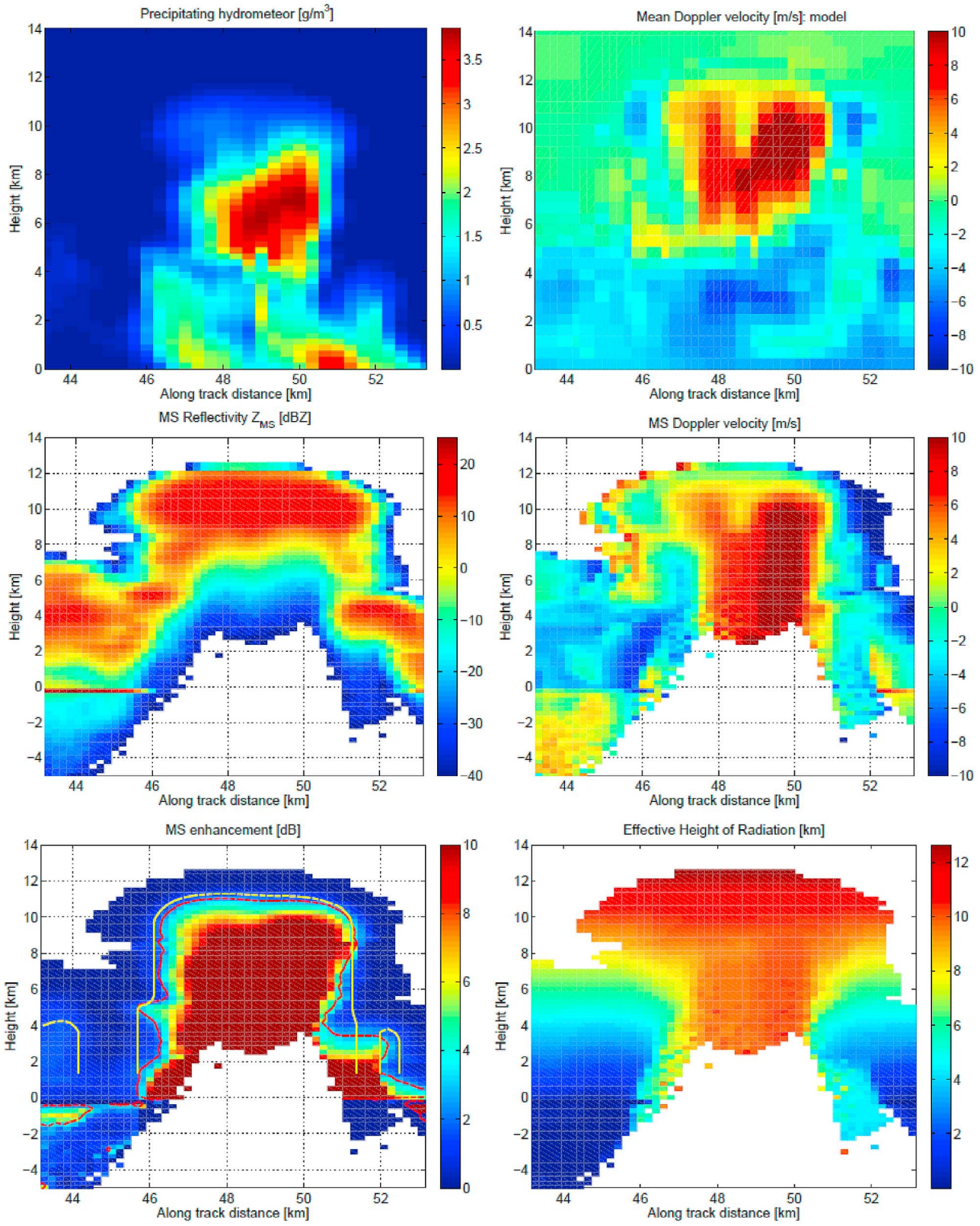

Figure 2. (top left) WRF model total hydrometeor content [g/m^3] and (top right) mean Doppler velocity [m s^{-1}]. (middle left) Simulated reflectivity and (middle right) mean Doppler velocity including all orders of scattering for the EarthCARE configuration. (bottom left) MS enhancement and (bottom right) effective radiation height ERH. In the bottom left panel the dashed red (yellow) line corresponds to the 3 *dB* contour level reflectivity enhancement ($\mathcal{H}_{MS}$ as identified by our criterion).

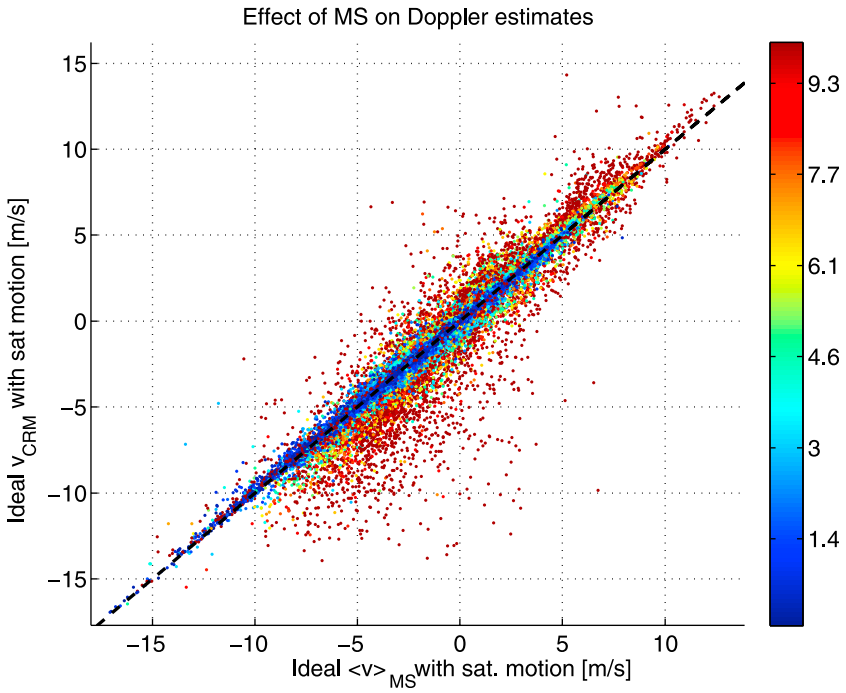

Figure 3. Mean Doppler velocity estimates. X-axis: estimates from Doppler spectra computed by the forward model including MS. *Y*-axis: *SS* estimates derived from the cloud resolving model output accounting for the radar footprint and the platform movement. The departure from the one-to-one line is caused purely by MS effects. The color is modulated by the MS enhancement ΔZ_{MS} expressed in dB and is capped at 10 dB (see colorbar).

surface MS can cause the absence of a surface return (e.g. at x = 51 km) as already noted by *Battaglia and Simmer* [2008]. In the convective core MS enhancement is ubiquitous for all the ranges below 10 km. As an indication of the height from where the returned power is generated it is useful to define the effective radiation height as:

$$ERH(r) \equiv \frac{\sum_{trajectories} \sum_{j} z Z_{obs}^{[j]}(z)}{\sum_{trajectories} \sum_{j} Z_{obs}^{[j]}(z)} \quad (1)$$

where $Z_{obs}^{[j]}$ is the contribution of the *j*th order of scattering to the observed radar reflectivity while z indicates the actual height where the *j*th order of scattering is occurring. Note that the first summation is extended only to the radiation 'trajectories' contributing to the same range bin (i.e. with apparent ranges between $r - \Delta r/2$ and $r + \Delta r/2$, Δr being the radar range resolution). *ERH* can be easily evaluated within the Monte Carlo procedure.

[18] For a perfectly nadir-pointing spaceborne system in *SS* regime *ERH* coincides with altitude $z = h_{sat} - r$; for spaceborne configuration $ERH(r) \geq z$, the larger the height-MS-displacement $\Delta\zeta_{MS} \equiv ERH(r) - z$ the more pronounced the *MS* effect. The bottom right panel of Figure 2 clearly demonstrates that the signal apparently coming from the middle of the convective core at around 8 km is generated by MS signal about 2 km above that altitude. In a nutshell, since radiation is not actually reaching down to that altitude it is not significantly contributing to the returned power; it is therefore obvious that no information about that altitude can be inferred directly from the apparent reflectivity. The simulated EC-CPR Doppler velocity (right middle panel) exhibits strong biases due to the along-track radar reflectivity inhomogeneity field (e.g. visible at the boundaries of the convective core). The impact of nonuniform beam filling on spaceborne Doppler velocity measurements has been already explored [*Tanelli et al.*, 2004]. Within the rain shaft, due to NUBF, down-draft motions can appear as up-drafts (for instance close to the ground around an along-track distance of 52 km). Second, as already noticed by *Battaglia and Tanelli* [2011] below the altitude where the MS contribution significantly overcomes the SS, the mean Doppler velocity of the backscattered signal departs from the mean Doppler velocity determined by the combined effect of the vertical-wind and hydrometeor-terminal velocities at all range bins. This is due to the above mentioned decoupling between the apparent range and the *ERH*.

[19] Figure 3 depicts the "ideal" (very large PRF) mean Doppler velocities as derived from the forward modeling (thus including MS contributions) versus the mean Doppler velocities as computed from the cloud resolving model accounting for the platform movement, i.e. the mean Doppler velocities expected in the SS approximation. As already noticed, the term ideal here refers to the fact that results are assumed to be unaffected by noise, or by sampling and/or aliasing problems. Therefore the departures from the one-to-one line represent the biases in the mean Doppler velocities introduced purely by MS effects. The scatterplot clearly shows that MS enhancements larger than 3 dB (cyan and warmer colors) have a huge impact in the reliability of mean Doppler velocity estimates, thus the

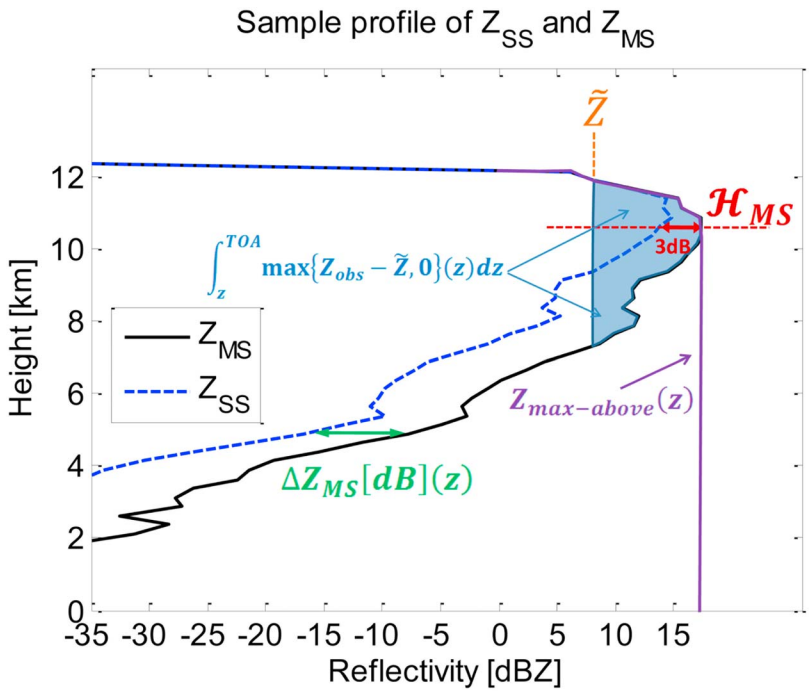

Figure 4. Example of simulated *SS* (blue) and MS (black) reflectivity profiles for deep convection as observed by a spaceborne nadir-looking 94 GHz radar. All variables defined in Section 4.1 are shown.

necessity of pre-flagging MS contaminated profiles. MS seems to produce a general tendency in mean Doppler velocity bias towards upward velocities. This is attributed, for these simulated profiles (see description later on in Section 4.2), to the presence of strong updrafts in the upper part of the convective cloud: these features are "stretched" along the profile due to the dwelling of the radiation in the upper layers (see, for instance, the convective core around 10 km height at 50 km integration distance, in the middle right panel of Figure 2). The MS effect is extremely detrimental when the MS enhancement exceeds 10 dB (red/brown dots).

4. Objective Determination of MS-Contaminated Radar Range-Bins

[20] The analysis of the previous case study demonstrated that recovering the actual Doppler velocity is particularly challenging in presence of convective clouds; in addition to the Doppler fading due to the fast satellite movement (and to the consequential folding into the Nyquist interval) and to nonuniform beam filling issues, the contamination by MS adds uncertainties to the problem. A careful characterization of the radar pixels that have significant contamination from MS is the first step. Linear depolarization ratio (LDR) measurements have been suggested as a method to identify MS contamination [*Battaglia et al.*, 2007]. Since LDR measurements are not available from the CloudSat and EarthCARE CPR's it is important to develop an alternative objective methodology for identifying MS contamination using the available radar reflectivity profile.

4.1. General Characterization of Reflectivities Profiles

[21] Given a generic radar reflectivity for each range bin centered at the height z, the following variables are defined (and depicted in Figure 4):

[22] The MS enhancement, i.e. the departure of the total observed return (that accounts for all orders of scattering) from the SS approximation, which can be computed only in a simulation framework (shown in Figure 4 as horizontal distance between SS and MS profile, green arrow), viz:

$$\Delta Z_{MS}[dB](z) \equiv Z_{MZ}(z)[dBZ] - Z_{SS}(z)[dBZ] \tag{2}$$

where Z_{MS} refers to the reflectivity computed accounting for all orders of scattering. The integral of the reflectivity above a certain threshold, $\tilde{Z}$, from the top of the atmosphere (TOA) down to level z:

$$\mathcal{I}(z)_{>\tilde{Z}} \equiv 10\ \log_{10}\left[\int_z^{TOA} \{Z_{obs} - \tilde{Z}\}(z)dz\right] \tag{3}$$

where the integral is performed only at those heights where $Z_{obs} > \tilde{Z}$ with threshold value subtracted. The integral (shaded area in Figure 4) is expressed in linear units [mm^6/m^2]. Recalling the definition of dBZ and following *Kulie et al.* [2010], we use dBZ_{int} as a unit for $10\log_{10}$ of this integrated reflectivity in mm^6/m^2. The maximum value of reflectivities above the given height:

$$Z_{max-above}(z) \equiv \max_{\tilde{z} \geq z}(Z_{obs}(\tilde{z})). \tag{4}$$

We assume the onset of MS as the level where $\Delta Z_{MS} \equiv 3dB$, i.e. where the contribution of second and successive orders of scattering are equal to the SS contribution. We will refer to the

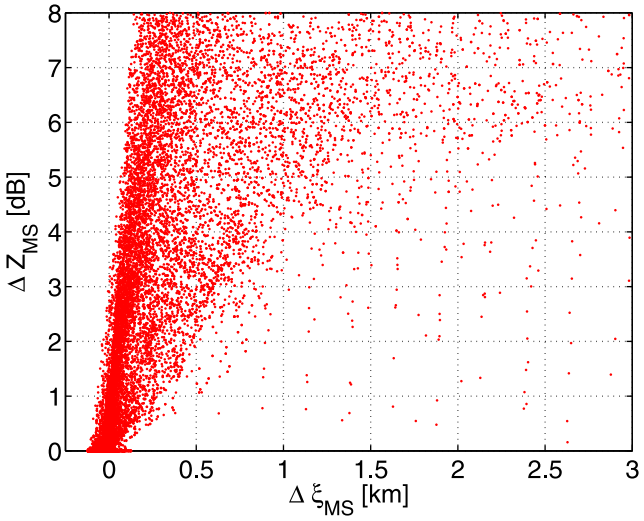

Figure 5. Scatterplot of $\Delta\zeta_{MS}$ versus ΔZ_{MS} for the simulated database for the EarthCARE configuration.

altitude where this condition is satisfied as the altitude of MS onset, $\mathcal{H}_{MS}$ (dashed red line in Figure 4). Extensive simulation have indicated that rarely radar range gates below this level are not contaminated by MS (it may occasionally happen in multilayer thick cloud situations). Thus, we assume that when MS contamination takes place it affects downward the whole profile. Above $\mathcal{H}_{MS}$ SS remains a valid approximation (see Figure 3) and the radar does have ranging capabilities. This is corroborated by Figure 5, which shows that with $\Delta Z_{MS} < 3dB$ the height-MS-displacement, $\Delta\zeta_{MS}$, remains below 250 m (half of the CloudSat and EC-CPR vertical resolution) for most of the cases.

4.2. Identification of Onset of Multiple Scattering

[23] In order to establish a criterion to determine $\mathcal{H}_{MS}$ the simulation framework described in Section 2 has been used. Note that in order to capture convection at different stages, a convective cell tracking algorithm adapted from *von Hardenberg et al.* [2003] had been used by *Parodi and Tanelli* [2010, Appendix A] to extract profiles which are more representative of the variety of natural observations. In this study we use a subset of the data set described therein; reflectivities for CloudSat and EC-CPR configurations have been simulated for more than 2000 convective profiles.

[24] Figure 6 depicts scatterplots of $Z_{\max-above}$ versus ΔZ_{MS} for the full data set in correspondence to the two radar configurations of Table 1. As expected, with increasing $Z_{\max-above}$ the MS enhancement becomes more and more pronounced. By visual inspection we can conclude that if $Z_{\max-above} < 8$ dBZ (12 dBZ) MS is not likely to have a large impact on the measured reflectivities in the CloudSat (EC) configuration. The different radar reflectivity thresholds reflect the larger CloudSat footprint. On the other hand when $Z_{\max-above}$ exceeds 8 dBZ (12 dBZ) MS can have a large impact on the observed radar reflectivity, however there are cases when the SS approximation can still be valid. The color of each scatter point in Figure 6 is modulated by the value of $\mathcal{I}(z)_{>8dBZ}$ and $I(z)_{>12dBZ}$ expressed in dBZ_{int}, respectively. The integrated reflectivity, from the top down to the level where MS is sought, can be used as a clustering variable. *Battaglia et al.* [2010] already propose that, for CloudSat configuration, the area subtended by the vertical reflectivity profile above the 8 dBZ threshold, $\mathcal{I}_{>8dBZ}$, can be adopted as a proxy for MS.

[25] This is further demonstrated in the top panel of Figure 7 which depicts the scatterplot in the $(\mathcal{I}(z), \Delta Z_{MS}(z))$ plane. Similarly to the procedure presented by *Battaglia et al.* [2008a] a fixed threshold value for the variable $I(z)_{>\tilde{Z}}$ divides the plane in four regions:

[26] 1. the upper left region where for the range pixel the SS approximation is wrongly appraised valid (missed detection);

[27] 2. the lower right region where the range pixel is falsely predicted to be contaminated by MS (false alarms);

[28] 3. the upper right region where the range pixel is correctly predicted to be contaminated by MS;

[29] 4. the lower left region where the range pixel is correctly predicted not to be contaminated by MS.

[30] For each of these regions the contingency tables with the number of hits of profiles which are (are not) MS con-

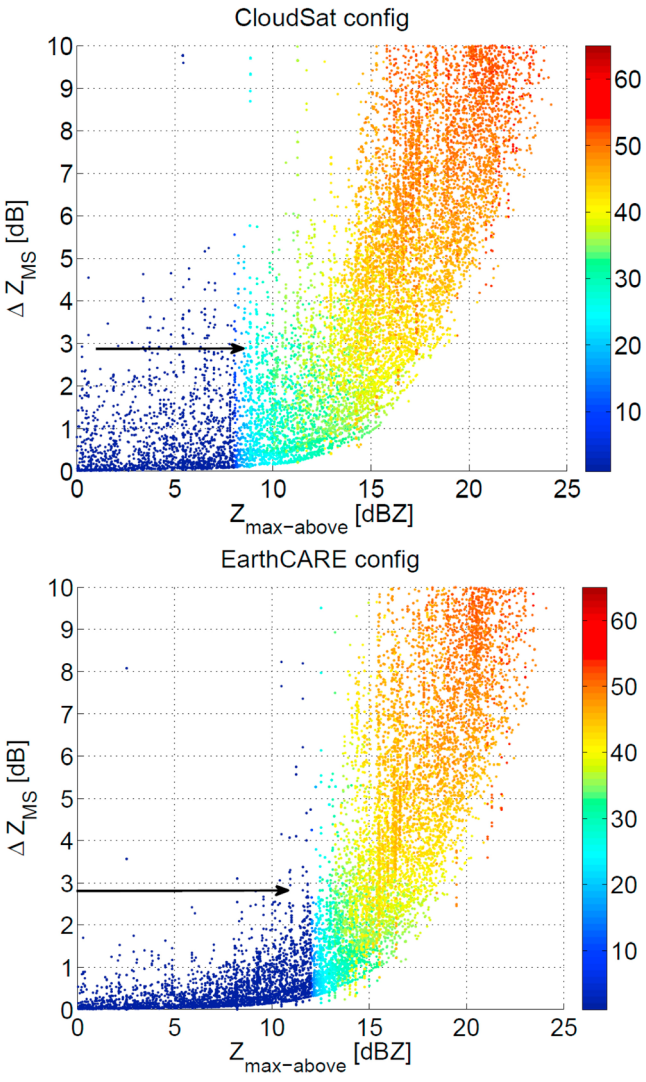

Figure 6. Scatterplot of $Z_{\max-above}$ versus ΔZ_{MS} for the simulated database for CloudSat (top) and EarthCARE (bottom) configuration.

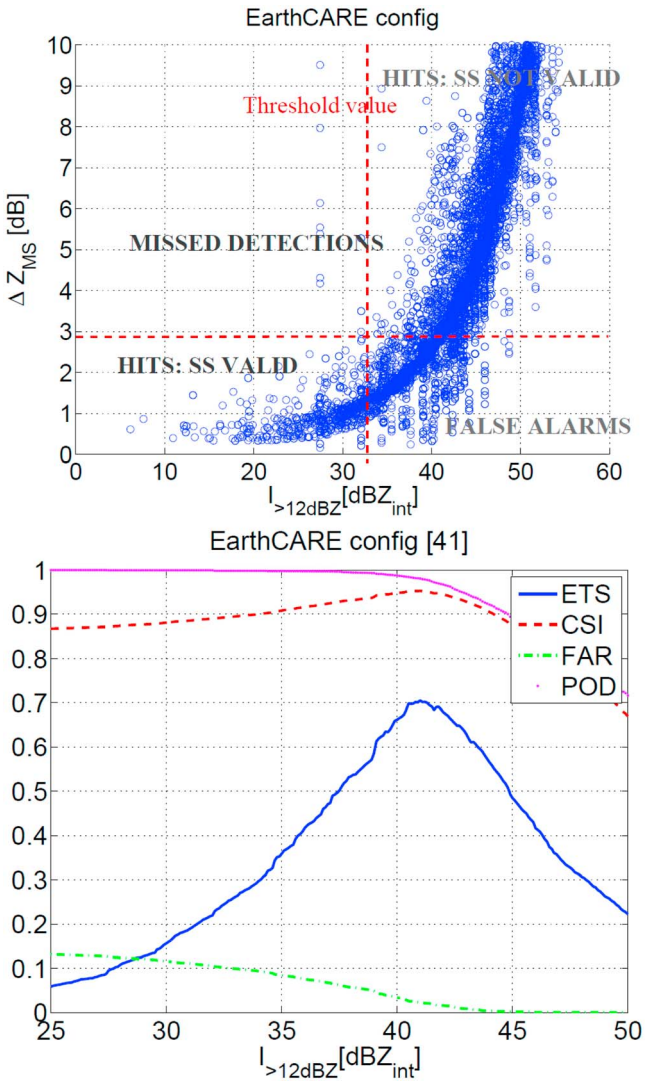

Figure 7. (top) Scatterplot of the integral quantity defined in equation (3) with threshold value $\tilde{Z}$ = 12 dBZ versus the MS enhancement. (bottom) Dependance of *ETS*, *CSI*, *FAR*, *POD* (as described in Section 4.2) on $I(z)_{>12dBZ}$ in the range from 25 to 50 dBZ_{int}.

taminated $N_A(N_D)$, the number of false alarms N_B, and the number of missed detections N_C are computed. From these parameters, knowing the expected number of correct forecasts due to chance $N_E = (N_A + N_C) \times (N_A + N_B)/N_T$ (where $N_T = N_A + N_B + N_C + N_D$ is the total number of range bins analyzed), the probability of detection $POD \equiv 1 - \frac{N_C}{N_T}$, the false alarm ratio $FAR \equiv \frac{N_B}{N_T}$, the critical success index $CSI \equiv \frac{N_A}{N_A+N_B+N_C}$ and the equitable threat score $ETS \equiv \frac{N_A-N_E}{N_A+N_B+N_C-N_E}$ are evaluated and are plotted in the bottom panel of Figure 7, having used $I(z)_{>12dBZ}$ in the range from 25 to 50 dBZ_{int}. For *ETS* the model gets penalized for forecasting outliers in the wrong place as well as not forecasting them in the right place; thus, the achievement of the best *ETS* generally corresponds to the best forecast skill. For the EarthCARE configuration the highest *ETS* value (0.7) is achieved in correspondence to $\mathcal{I}(z)_{>12dBZ}$ = 41 dBZ_{int} (0.61 at $\mathcal{I}(z)$ = 46 dBZ_{int}). For the CloudSat configuration (not shown) similar conclusions are drawn with a maximum *ETS* of 0.67 reached in correspondence of $I(z)_{>8dBZ}$ = 41.9 dBZ_{int} ($\mathcal{I}(z)$ = 44.3 dBZ_{int}). Below $\mathcal{I}(z)$ = 30 dBZ_{int} there is no sign of MS.

[31] In summary, the identification of MS onset simply relies on the following procedure:

[32] 1. identification of deep convective profiles;

[33] 2. computation of $\mathcal{I}(z)_{\tilde{Z}}$;

[34] 3. identification of the level, $\mathcal{H}_{MS}$, where $\mathcal{I}(z)_{\tilde{Z}}$ reaches its critical value.

5. CloudSat Convective Profile Analysis: A Case Study and Global Statistics

[35] The procedure can be easily applied to CloudSat observations. Step 1 of the procedure is facilitated by the 2B-CLDCLASS product (http://www.cloudsat.cira.colostate.edu/dataSpecs.php), where CloudSat profiles are classified into eight basic cloud types [*Sassen and Wang*, 2008] based on quantities like hydrometeor vertical and horizontal scales, the maximum Z_{obs} measured by the CPR, indications of precipitation, and ancillary data including predicted ECMWF temperature profiles and surface topography height. Two cloud types of particular importance to this study are nimbostratus (Ns) and deep convection, which extends from the surface to the upper troposphere and shows high precipitation intensity. To further avoid contamination from not-deep convective clouds, our analysis is limited to clouds having already exceeded the 0-dBZ level above 10 km.

[36] CloudSat reflectivity profiles and the 2B-CLDCLASS cloud classification flags for a convective core observed over Brazil during the descending orbit on the 19th of November, 2009 at about 5:20 UTC are depicted in Figure 8. Indices above 15 correspond to deep convective clouds, 1 to clear sky, 2 to cirrus, 4 to altostratus, 5 to altocumulus, 8 to stratus, 10 to stratocumulus, 12 to cumulus. The convective core is clearly identified by the dark red area of the 2B-CLDCLASS classification index (top panel). Our MS criterion can be applied to the convective core and identifies the onset of MS (dashed black line). At the very center of the overshooting top the SS theory is believed to be valid for this CloudSat observation only down to 13 km while at the side of the convective tower $\mathcal{H}_{MS}$ decreases to about 9 km. It is noticeable that below the $\mathcal{H}_{MS}$ level (dashed black line) all conclusions drawn on the basis of SS theory (e.g. all 2B-CWC-RO and 2C-PRECIP-COLUMN products) are likely to be subject to large errors in the radar reflectivity due to MS contamination.

[37] CloudSat observations from July 2007 and January 2008 have been used to produce a statistics of how deep the CloudSat CPR can sense convective cores. On average 4.4% of the total number of CloudSat profiles are identified as belonging to convective cores according to the two following criteria: 1) cloud class index ≥15; 2) reflectivity exceeding 0-dBZ above 10 km. A contour frequency altitude display (CFAD) for the selected profiles is shown in Figure 9. Profiles are always characterized by decreasing reflectivity in the lowest 6–8 kilometers, a clear signature of attenuation in the lowest layers due to the strong precipitation; however, in these layers, attenuation is believed to be substantially compensated by MS. For every profile the height of the −20 dBZ contour and the height of the MS onset, $\mathcal{H}_{MS}$, are computed. The histogram of $\mathcal{H}_{MS}$ shown in

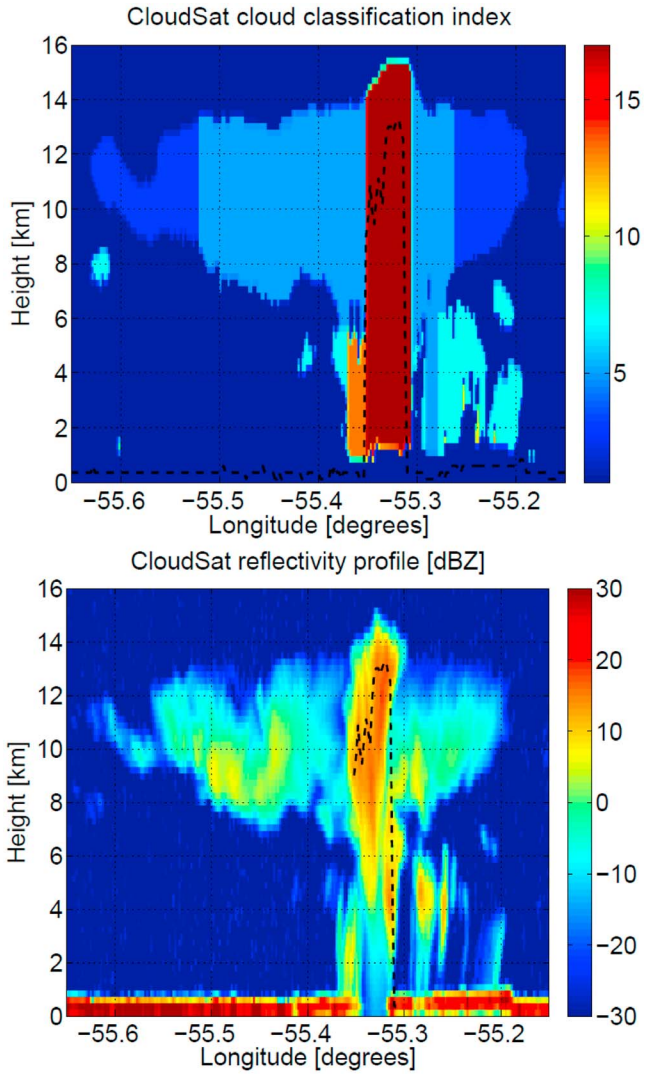

Figure 8. (top) CloudSat cloud classification index as introduced in Section 5 and (bottom) reflectivity profile for a convective core observed by CloudSat on November 19th, 2009 at about 5:20 UTC above Brazil. The black dashed line indicates $\mathcal{H}_{MS}$: below that level MS is believed to play a key, nonnegligible role.

the top panel of Figure 10 demonstrates that only a very small fraction (5%) of the convective cores is not affected by MS at all (i.e. their $\mathcal{H}_{MS}$ is equal zero). On the other hand, profiles affected by MS have an average $\mathcal{H}_{MS}$ close to 9.5 km. These findings agree with the conclusions drawn by *Bouniol et al.* [2008] for their case study during AMMA (see their Figure 8). On the other hand the penetration depth seems to gradually increase with the −20-dBZ-level cloud height (bottom panel). For very tall systems a penetration of even 7–8 kilometers seems feasible. Due to its smaller footprint compared to CloudSat, EC is clearly going to improve in that respect.

[38] This analysis reveals that a significant region of the convective cores can still be investigated with *W*-band radars by exploiting SS theory. In convective cores, considering only the pixels between the −20-dBZ-level cloud height and the freezing level height, on average 34% of the pixels are not affected by MS in CloudSat configuration. Extrapolating the analysis for the EarthCARE mission more than 40% of the observations of deep convection cores above the freezing level are deemed to bring useful information that can be interpreted with SS theory. Therefore, studies for the assessment of the feasibility and the accuracy of Doppler estimates for such regions are meaningful.

6. Discussion and Conclusions

[39] Doppler velocity measurements from spaceborne *W*-band Doppler radars are particularly challenging in presence of convective clouds. In addition to the Doppler fading due to the fast satellite movement and to nonuniform beam filling issues, the contamination by MS adds additional uncertainties. Based on a simulation framework, a criterion to identify the MS onset in *W*-band radar observations has been derived for two typical configurations (the one currently operated in the CloudSat mission and that envisaged for the EarthCARE mission). The cumulative integrated reflectivity from the top of the atmosphere (defined in equation (3)) is used as a proxy for enhanced MS contamination; a proper configuration-dependent threshold is selected based on a statistical analysis which maximizes the equitable threat score. Compared to previous approaches, the added value is the exploitation of purely-reflectivity-profile-derived quantities to detect the onset of MS. For the CloudSat configuration, a statistical analysis conducted on two months of data reveals that the great majority of the profiles (95%) within convective cores are affected by MS, with the onset of MS located in the region between 9–10 km. Considering only the pixels between −20-dBZ-level cloud height and the freezing level height, on average, 35% of the pixels are not affected by MS. The identification of the region where MS plays a crucial role is utterly important, and currently developed products based on SS theory like 2B-CWC-RO and 2B-CWC-RVOD should account for it in order to avoid misleading conclusions

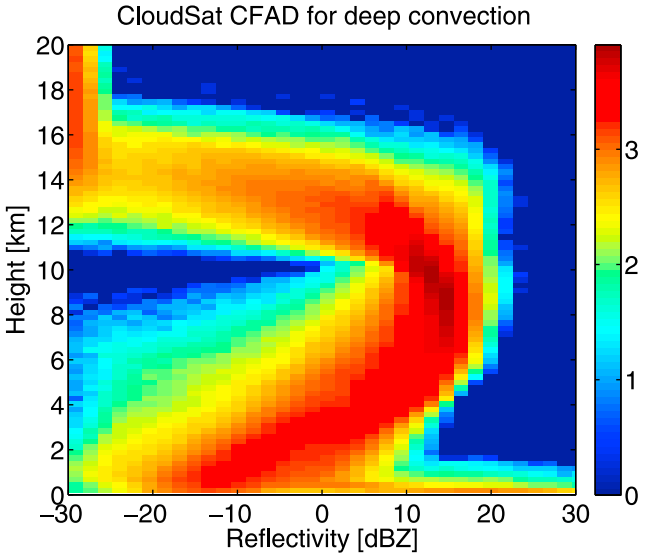

Figure 9. Contour Frequency Altitude Display for CloudSat observed reflectivities profiles of deep convection. The colorbar modulates the $\log_{10}$ of number of occurrences.

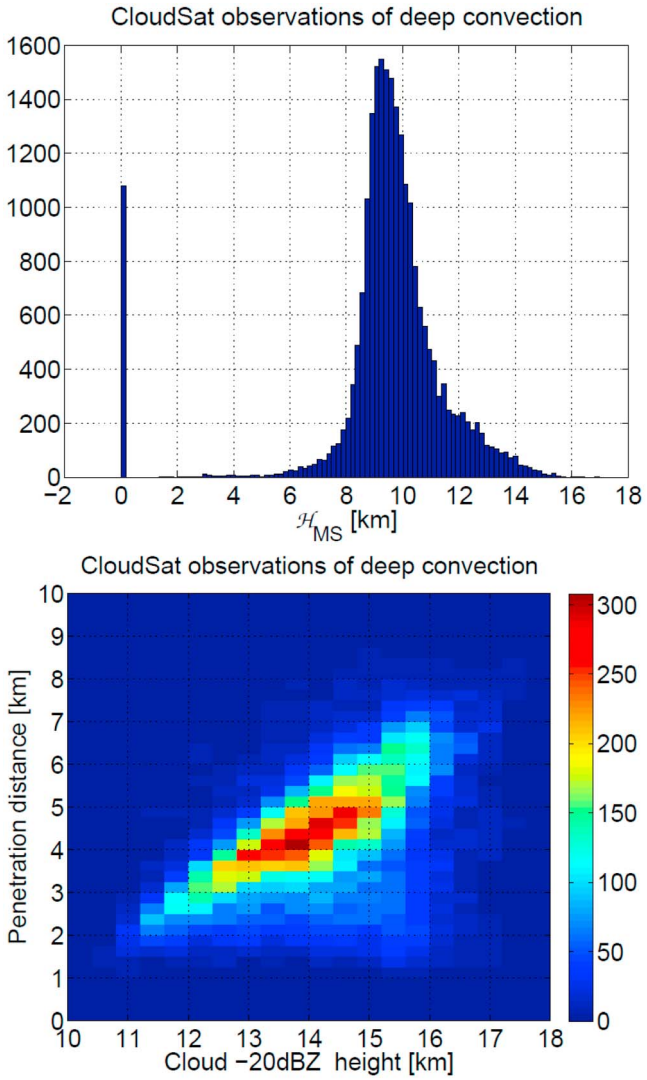

Figure 10. (top) Histogram of the altitude of MS onset, H_{MS}, for the CloudSat data set of convective core observations identified according to the criteria described in Section 5. (bottom) Number of occurrences (color coded) of CloudSat convective core profiles as a function of the −20-dBZ-level and the penetration depth. This latter quantity is defined as the difference between the −20-dBZ-level and the altitude of MS onset.

about ice particle sizes, contents and radiative fluxes in deep convective cores.

[40] A fortiori, for the EarthCARE mission it is likely that more than 40% of the observations of deep convection cores above the freezing level may bring useful information that can straightforwardly be interpreted with SS theory. Studies assessing the feasibility and the accuracy of Doppler estimates within such regions are currently ongoing and are expected to provide a quantitative assessment of the ability of the EC-CPR to recover Doppler velocities in deep convection, a key scientific requirement of the EarthCARE mission.

[41] The objective methodology discussed in this paper is only valid for deep convective cores. Shallower convective and stratiform precipitating clouds are also believed to be burdened by MS effects (for instance in the bottom left panel of Figure 2 our criterion clearly misdefine the onset of MS for the convective core at around 44 km along track distance). Because of the completely different microphysics of the vertical profiles present in such conditions, separate studies are now planned to extend the present criterion to these other precipitating regimes.

[42] **Acknowledgments.** This work was supported by the European Space Agency under the Doppler Air Motion Estimate project funded by the STSE program. A. Battaglia's travel and publication costs were covered by the NCEO EO Mission Support. The contributions by Simone Tanelli were performed at the Jet Propulsion Laboratory under contract with the National Aeronautics and Space Administration. Support for the "Instrument Simulator Suite for Atmospheric Remote Sensing" project from the Advanced Information Systems Technology Program, and for the "Doppler Velocity Products for the EarthCARE mission" from the NASA SALMON/USPI program are gratefully acknowledged. The financial and educational support of the Department of Physics and Astronomy, University of Leicester for Augustynek's Ph.D. are also greatly acknowledged.

References

Battaglia, A., and C. Simmer (2008), How does multiple scattering affect the spaceborne W-band radar measurements at ranges close to and crossing the sea-surface range?, *IEEE Trans. Geosci. Remote Sens.*, *46*(6), 1644–1651.

Battaglia, A., and S. Tanelli (2011), DOMUS: Doppler Multiple Scattering Simulator, *IEEE Trans. Geosci. Remote Sens.*, *49*(1), 442–450, doi:10.1109/TGRS.2010.2052818.

Battaglia, A., M. O. Ajewole, and C. Simmer (2007), Evaluation of radar multiple scattering effects in CloudSat configuration, *Atmos. Chem. Phys.*, *7*, 1719–1730.

Battaglia, A., J. M. Haynes, T. L'Ecuyer, and C. Simmer (2008a), Identifying multiple-scattering affected profiles in CloudSat observations over the oceans, *J. Geophys. Res.*, *113*, D00A17, doi:10.1029/2008JD009960.

Battaglia, A., S. Kobayashi, S. Tanelli, E. Im, and C. Simmer (2008b), Multiple scattering effects in pulsed radar systems: An intercomparison study, *J. Atmos. Oceanic Technol.*, *25*(9), 1556–1567, doi:10.1175/2008JTECHA1023.1.

Battaglia, A., S. Tanelli, S. Kobayashi, D. Zrnic, R. J. Hogan, and C. Simmer (2010), Multiple-scattering in radar systems: A review, *J. Quant. Spectrosc. Radiat. Transfer*, *111*, 917–947, doi:10.1016/j.jqsrt.2009.11.024.

Bouniol, D., A. Protat, A. Plana-Fattori, J.-P. Vinson, M. Giraud, and N. Grand (2008), Comparison of airborne and spaceborne 95-GHz radar reflectivities and evaluation of multiple scattering in spacebourne measurements, *J. Atmos. Oceanic Technol.*, *25*(11), 1983–1995, doi:10.1175/2008JTECHA1011.1.

Chung, E. S., B. J. Sohn, and J. Schmetz (2008), CloudSat shedding new light on high-reaching tropical deep convection observed with Meteosat, *Geophys. Res. Lett.*, *35*, L02814, doi:10.1029/2007GL032516.

Corti, T., et al. (2008), Unprecedented evidence for deep convection hydrating the tropical stratosphere, *Geophys. Res. Lett.*, *35*, L10810, doi:10.1029/2008GL033641.

Haynes, J. M., T. S. L'Ecuyer, G. L. Stephens, S. D. Miller, C. Mitrescu, N. B. Wood, and S. Tanelli (2009), Rainfall retrieval over the ocean with spaceborne W-band radar, *J. Geophys. Res.*, *114*, D00A22, doi:10.1029/2008JD009973.

Iwasaki, S., T. Shibata, J. Nakamoto, H. Okamoto, H. Ishimoto, and H. Kubota (2010), Characteristics of deep convection measured by using the A-train constellation, *J. Geophys. Res.*, *115*, D06207, doi:10.1029/2009JD013000.

Jensen, E. J., A. S. Ackerman, and J. A. Smith (2007), Can overshooting convection dehydrate the tropical tropopause layer?, *J. Geophys. Res.*, *112*, D11209, doi:10.1029/2006JD007943.

Kollias, P., E. E. Clothiaux, M. A. Miller, B. A. Albrecht, G. L. Stephens, and T. P. Ackerman (2007), Millimeter-wavelength radars: New frontier in atmospheric cloud and precipitation research, *Bull. Am. Meteorol. Soc.*, *88*(10), 1608–1624, doi:10.1175/BAMS-88-10-1608.

Kuang, Z., and C. S. Bretherton (2004), Convective influence on the heat balance of the tropical tropopause layer: A cloud-resolving model study, *J. Atmos. Sci.*, *61*(23), 2919–2927, doi:10.1175/JAS-3306.1.

Kulie, M. S., R. Bennartz, T. J. Greenwald, Y. Chen, and F. Weng (2010), Uncertainties in microwave properties of frozen precipitation: Implications for remote sensing and data assimilation, *J. Atmos. Sci.*, *67*(11), 3471–3487, doi:10.1175/2010JAS3520.1.

Liu, C., and E. J. Zipser (2005), Global distribution of convection penetrating the tropical tropopause, *J. Geophys. Res.*, *110*, D23104, doi:10.1029/2005JD006063.

Liu, C., E. J. Zipser, and S. W. Nesbitt (2007), Global distribution of tropical deep convection: Different perspectives from TRMM infrared and radar data, *J. Clim.*, *20*(3), 489–503, doi:10.1175/JCLI4023.1.

Liu, C., E. J. Zipser, D. J. Cecil, S. W. Nesbitt, and S. Sherwood (2008), A cloud and precipitation feature database from nine years of TRMM observations, *J. Appl. Meteorol. Climatol.*, *47*(10), 2712–2728.

Luo, Z., G. Y. Liu, and G. L. Stephens (2008), CloudSat adding new insight into tropical penetrating convection, *Geophys. Res. Lett.*, *35*, L19819, doi:10.1029/2008GL035330.

Parodi, A., and S. Tanelli (2010), Influence of turbulence parameterizations on high-resolution numerical modeling of tropical convection observed during the TC4 field campaign, *J. Geophys. Res.*, *115*, D00J14, doi:10.1029/2009JD013302.

Protat, A., D. Bouniol, J. Delanoë, E. O'Connor, P. T. May, A. Plana-Fattori, A. Hasson, U. Görsdorf, and A. J. Heymsfield (2009), Assessment of CloudSat reflectivity measurements and ice cloud properties using ground-based and airborne cloud radar observations, *J. Atmos. Oceanic Technol.*, *26*(9), 1717–1741, doi:10.1175/2009JTECHA1246.1.

Sassen, K., and Z. Wang (2008), Classifying clouds around the globe with the CloudSat radar: 1-year of results, *Geophys. Res. Lett.*, *35*, L04805, doi:10.1029/2007GL032591.

Schutgens, N. A. J. (2008a), Simulated Doppler radar observations of inhomogeneous clouds: Application to the EarthCARE space mission, *J. Atmos. Oceanic Technol.*, *25*(1), 26–42, doi:10.1175/2007JTECHA956.1.

Schutgens, N. A. J. (2008b), Simulating range oversampled Doppler radar profiles of inhomogeneous targets, *J. Atmos. Oceanic Technol.*, *25*(9), 1514–1528, doi:10.1175/2007JTECHA1026.1.

Sherwood, S. C., and A. E. Dessler (2001), A model for transport across the tropical tropopause, *J. Atmos. Sci.*, *58*(7), 765–779, doi:10.1175/1520-0469.

Sherwood, S. C., J.-H. Chae, P. Minnis, and M. McGill (2004), Underestimation of deep convective cloud tops by thermal imagery, *Geophys. Res. Lett.*, *31*, L11102, doi:10.1029/2004GL019699.

Sirmans, D., and B. Bumgarner (1975), Numerical comparison of five mean frequency estimators, *J. Appl. Meteorol.*, *14*(6), 991–1003, doi:10.1175/1520-0450(1975)014<0991:NCOFMF>2.0.CO;2.

Skamarock, W. C., J. B. Klemp, J. Dudhia, D. O. Gill, D. M. Barker, W. Wang, and J. G. Powers (2005), A description of the Advanced Research WRF Version 2, *Tech. Rep. NCAR/TN-468+STR*, 88 pp., NCAR, Boulder, Colo.

Sohn, B.-J., and J. Schmetz (2004), Water vapor-induced OLR variations associated with high cloud changes over the Tropics: A study from Meteosat-5 observations, *J. Clim.*, *17*(10), 1987–1996, doi:10.1175/1520-0442(2004)017<1987:WVOVAW >2.0.CO;2.

Stephens, G. L., et al. (2008), CloudSat mission: Performance and early science after the first year of operation, *J. Geophys. Res.*, *113*, D00A18, doi:10.1029/2008JD009982.

Tanelli, S., E. Im, S. L. Durden, L. Facheris, and D. Giuli (2002a), The effects of nonuniform beam filling on vertical rainfall velocity measurements with a spaceborne Doppler radar, *J. Atmos. Oceanic Technol.*, *19*(7), 1019–1034, doi:10.1175/1520-0426(2002)019<1019:TEONBF>2.0.CO;2.

Tanelli, S., E. Im, L. Facheris, and E. A. Smith (2002b), DFT-based spectral moments estimators for spaceborne Doppler precipitation radar, *Proc. SPIE Int. Soc. Opt. Eng.*, *4894*(50), 218, doi:10.1117/12.467754.

Tanelli, S., E. Im, S. L. Durden, L. Facheris, D. Giuli, and E. A. Smith (2004), Rainfall Doppler velocity measurements from spaceborne radar: Overcoming nonuniform beam-filling effects, *J. Atmos. Oceanic Technol.*, *21*(1), 27–44, doi:10.1175/1520-0426(2004)021<0027:RDVMFS>2.0.CO;2.

Tanelli, S., E. Im, S. Kobayashi, R. Mascelloni, and L. Facheris (2005), Spaceborne Doppler radar measurements of rainfall: Correction of errors induced by pointing uncertainties, *J. Atmos. Oceanic Technol.*, *22*(11), 1676–1690, doi:10.1175/JTECH1797.1.

Tanelli, S., S. L. Durden, E. Im, K. S. Pak, D. G. Reinke, P. Partain, J. M. Haynes, and R. T. Marchand (2008), CloudSat's cloud profiling radar after two years in orbit: Performance, calibration, and processing, *IEEE Trans. Geosci. Remote Sens.*, *46*(11), 3560–3573.

Tian, B., and V. Ramanathan (2002), Role of tropical clouds in surface and atmospheric energy budget, *J. Clim.*, *15*(3), 296–305, doi:10.1175/1520-0442(2002)015<0296:ROTCIS>2.0.CO;2.

von Hardenberg, J., L. Ferraris, and A. Provenzale (2003), The shape of convective rain cells, *Geophys. Res. Lett.*, *30*(24), 2280, doi:10.1029/2003GL018539.

Voors, R., et al. (2007), ECSIM: The simulator framework for EarthCARE, *Proc. SPIE Int. Soc. Opt. Eng.*, 67441Y, doi:10.1117/12.737738.

Zrnić, D. S. (1975), Simulation of weatherlike Doppler spectra and signals, *J. Appl. Meteorol.*, *14*(4), 619–620, doi:10.1175/1520-0450(1975)014<0619:SOWDSA>2.0.CO;2.

T. Augustynek and A. Battaglia, Department of Physics and Astronomy, University of Leicester, University Road, Leicester LE17RH, UK. (a.battaglia@le.ac.uk)

P. Kollias, Department of Atmospheric and Oceanic Sciences, McGill University, 805 Sherbrooke St. W., Montreal, QC H3A 2K6, Canada.

S. Tanelli, Jet Propulsion Laboratory, California Institute of Technology, 4800 Oak Grove Dr., MS 300-243, Pasadena, CA 91109, USA.